Journal Name

Dynamic Article Links ▶

ARTICLE TYPE

Enhanced thermoelectric properties of the *n*-type Magnéli phase WO$_{2.90}$: Reduced thermal conductivity through microstructure engineering

Gregor Kieslich[a], Ulrich Burkhardt[b], Christina S. Birkel[c,d], Igor Veremchuk[b], Jason E. Douglas [c,e], Michael W. Gaultois[c,d], Ingo Lieberwirth[f], Ram Seshadri[c,d,e], Galen D. Stucky[c,d], Yuri Grin[b]*, and Wolfgang
5 Tremel[a]*

The thermoelectric properties of the Magnéli phase WO$_{2.90}$ were investigated, with special attention to how the thermoelectric
10 performance can be altered by changing its microstructure. Spark plasma sintering (SPS) allowed the direct preparation of large amounts of consolidated material. Adding Ta$_2$O$_5$ to the reaction mixture lead to the formation of solid solutions W$_{1-x}$Ta$_x$O$_{2.90}$ via a concurrent reaction between WO$_3$ and Ta$_2$O$_5$ the during SPS treatment. In addition, micro-size inclusions containing tungsten surrounded by a WO$_x$ embedded in a WO$_{2.90}$ matrix were formed, which act as additional scattering centers. As a result, the thermal conductivity of the Ta-containing samples was reduced by ≈30% over the temperature range from 300 to 1100 K while the
15 electronic properties remained unaffected, which in turn enhanced the thermoelectric performance and lead to a relatively high zT value of 0.15 at 1100 K for n-type metal oxides.

Introduction

Interfacial scattering over a wide range of length scales is an
20 efficient approach to enhance thermoelectric performance.[1,2] In this context, many activities have focused on dense materials based on sintered nanoparticles,[3,4] artificially structured superlattices,[5] or materials containing nanosegregations.[6] In these systems the lattice part of the thermal conductivity is decreased
25 owing to enhanced phonon scattering at particle interfaces,[7,8] which leads to an increased thermoelectric figure of merit, $zT = (\alpha^2\sigma/\kappa)\cdot T$, with thermopower α, electrical conductivity σ, thermal conductivity κ, and absolute temperature T. State of the art chalcogenide-based thermoelectric materials like PbTe,[2,9,10] AgPb$_m$S-
30 bTe$_{m+2}$,[11,12] and Bi$_2$Te$_3$[13–15] contain scattering centers at different length scales (atomic scale, nanoscale and microscale). Another way to additionally reduce the intrinsic thermal lattice conductivity is based on the formation of spatially separated regions with different types of chemical bonding, which was observed (in the
35 2 dimensional case) for Bi$_2$Te$_3$[13-15] or the 3 dimensional case for Ba$_8$Au$_{5.3}$Ge$_{40.7}$.[16]

The quest for new stable and sustainable thermoelectric materials with earth-abundant, non-toxic, and cheap component elements that allow tuning the thermoelectric properties over a wide range
40 for large-scale applications prompted us to explore metal oxides with intrinsic nanostructures, predefined by the structural motifs of the respective compounds.[3,17-20] In this context, the so-called Magnéli-type oxides have gained attention because of crystallographic shear planes,[21–23] a large number of atoms in the unit cell
45 and good and tuneable electrical conductivity.[24] The crystallographic shear planes form a layer-like intergrowth structure (Fig.

1), which is believed to be responsible for their low lattice thermal conductivities of 3-4 W m^{-1} K^{-1}.[25] The crystallographic shear planes act as scattering centers for phonons without disrupting
50 electron transport. Large unit cells are attractive, as it is known that a large number of atoms in the unit cell lead to low lattice thermal conductivities κ_L in oxides and intermetallic compounds because of the low velocity of optical phonon modes.[26–31] This trend of a large atom number and low κ_L can be qualitatively
55 understood within the periodic boundary conditions of a monoatomic chain described elsewhere.[30,32]
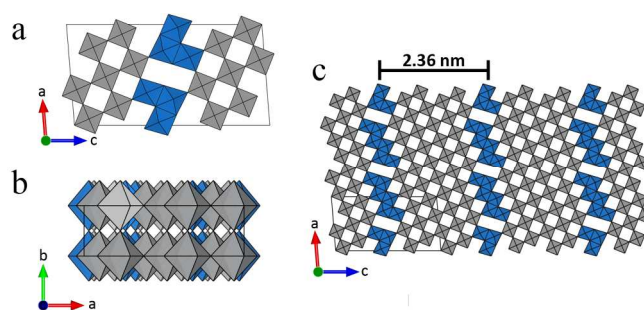
Fig. 1. Crystal structure of WO$_{2.90}$ viewed along [010] (a) and [001] (b).
60 The intergrowth structure is associated with crystallographic shear planes (c). The Magneli-type structure can be interpreted as a 1D stacking of the WO$_3$ building blocks (light grey) separated by layers of edge-shared octahedral (blue).

Most complex metal oxides are electrical insulators, such as
65 Y$_3$Al$_5$O$_{12}$,[33] La$_2$Mo$_2$O$_9$,[34] and W$_3$Nb$_{14}$O$_{44}$,[35] the latter being structurally related to the Magnéli-type oxides. However, the presence of mixed valence states due to a partial reduction of M^{6+} to M^{5+}

(e.g. M = W^{5+}, Mo^{5+}) and the accompanying crystallographic shear lead to the appearance of free carriers and therefore quasi-metallic electrical conductivity. Magnéli-type oxides show some promise to close the current gap of the thermoelectric performance between *n*-type and *p*-type oxides. Today ZnO and $SrTiO_3$, which have been studied for more than 20 years in the context of thermoelectric research, are the best characterized *n*-type oxides with current state of the art *zT* values of ~ 0.6 ($Zn_{1-x-y}Al_xGa_yO$) and ~0.15 (nanostructured $SrTiO_3$).[36,37] The reported *zT* values of 0.1 (for SPS processed $WO_{2.90}$) and 0.13 (for conventionally prepared $WO_{2.90}$) at 1100 K[25,33] indicate the potential of this group of compounds for thermoelectrics.

This contribution focuses on the optimization of the thermal transport properties of the binary Magnéli phase $WO_{2.90}$, where {103} crystallographic shear planes have been identified by crystal structure determination[21,34] (Fig. 1). This compound is a heavily doped semiconductor with *n*-type charge carriers.[24,25,35] In the pure compound, crystallographic shear planes and disorder on a length scale > 5 nm are the principal scattering centres. Although oxygen loss and further reduction processes are known to occur at high temperatures that go along with a structural rearrangement in Magnéli phases, $WO_{2.90}$ shows a cycling stability between room temperature and 1100 K.[33] The thermal stability of $WO_{2.90}$ was demonstrated up 700°C.[38] We demonstrate here that the thermal conductivity of $WO_{2.90}$ can be decreased by increasing the complexity of the microstructure through the addition of Ta_2O_5 as a heterocomponent, which leads to the formation of additional scattering centres while conserving the electronic properties of the parent compound. Thus, interfacial scattering on different length scale is used to increase the thermoelectric figure of merit in these oxides. Detailed metallographic studies were performed, which provide comprehensive insight into the microstructure-property relationship.

Experimental

Synthesis. Stoichiometric amounts of W, WO_3 and Ta_2O_5 (Sigma Aldrich, particle size < 20 μm) were thoroughly ground and loaded into a graphite die with an inner diameter of 20 mm. Spark plasma sintering (SPS) was used to simultaneously prepare and consolidate the $WO_{2.90}$ as described in detail previously.[33] SPS treatments were performed on a SPS – HP D 5 setup (FCT, Germany). Prior to heating, an uniaxial pressure of 50 MPa was applied. Subsequently, the material was heated rapidly to 1473 K at 100 K min^{-1}. After a holding time of 5 min and cooling to room temperature, the cylindrical pellet was removed from the die and polished with SiC grinding paper to obtain a clean surface free from carbon foil and any potential carbides that could have formed.

Measurements. For the measurement of the electronic properties, bar-shaped pieces with the approximate dimensions of 12 mm × 2 mm × 2 mm were cut using a low-speed saw (Allied Inc.) with a diamond wafering blade. Seebeck coefficient and electrical resistivity in the temperature region between 300 K and 1100 K were measured simultaneously on those specimens using a ZEM-3 Ulvac instrument. The current direction was perpendicular to the pressure axis of SPS.

To carry out thermal diffusivity measurements, disks (7.5 mm in diameter and 2 mm in thickness) were cut by wire electrical

discharge machining (EDM, BROTHER HS-350) and sprayed with a layer of carbon paint in order to minimize errors in the emissivity. The thermal diffusivity was measured on compacted discs along the pressure axis of the SPS with a Netzsch laser flash diffusivity instrument, LFA 457. The data were analyzed using a Cowan model with pulse correction. Specific heat measurements were performed on a Netzsch Pegasus differential scanning calorimeter (DSC). The specimens were heated up to 1073 K under Ar atmosphere with a heating rate of 10 K min^{-1}. The sample density was calculated from the measured mass-to-volume ratio, and the thermal conductivity was calculated as $\kappa = D \cdot \rho \cdot C$, where *D* is the diffusivity, *ρ* the density and *C* the heat capacity. The experimental densities were determined as 96% and 98% of the theoretical density of $WO_{2.90}$ ($\rho = 7.17 g\ cm^{-3}$). The Debye function was fitted numerically to the heat capacity to extract the Debye temperature.[33]

Field-emission scanning electron microscopy was performed on a FEI XL40 Sirion FEG microscope with an attached Oxford Inca X-ray system for chemical analysis. After polishing, the samples (mounted in epoxy) were coated with silver paste in order to prevent the sample from charging during imaging. Secondary and backscattered electron images were collected with acceleration voltages of 5 keV and 15 or 20 keV, respectively.

Line scans have been performed on an electron microprobe CAMECA SX 100 (W-cathode) and on a SEM XL30 (FEI, LaB_6 cathode). The intensities of the X-ray lines W Lα, Ta Lα, and O K were recorded on the microprobe by a wavelength spectrometer with LiF and Ni/C multilayer monochromator crystals, respectively. Acceleration voltages of 25 kV or 10 kV were used for the analyses of the transition metal or oxygen concentrations, respectively. An acceleration voltage of 7 kV was used for the measurements with the EDXS system (Bruker, SDD XFlash 6/30, Quantax Software). The background-subtracted net-intensities of the X-ray lines W M, Ta M and O K lines were recorded.

High resolution transmission microscopy (HR-TEM) was performed on a FEI Tecnai F30 S-TWIN transmission electron microscope equipped with a field emission gun. Samples were cut with a diamond knife in a Leica ultra-cut UCT and transferred onto lacey TEM grids.

Powder X-ray diffraction (PXRD) was performed with the X-ray Guinier diffraction technique (Huber G670 camera, $CrK_{\alpha1}$ radiation, λ = 2.2897 Å, graphite monochromator, $5° \leq 2\theta \leq 100°$, $\Delta 2\theta = 0.005°$). The positions of the reflection were determined by profile fitting; the unit cell parameters were calculated from a least-square refinement as LaB_6 internal standard.[39]

Results and Discussion

Four powder mixtures of WO_3 and W with respective ratio (equation 1) were prepared without and with adding Ta_2O_5 powder (3–5 mass %). The primary reaction observed during the SPS procedure is

$$2.9\ WO_3 + 0.1\ W = 3\ WO_{2.90} \qquad (1)$$

Besides the target phase $WO_{2.90}$ another Magnéli phase $WO_{2.96}$[40] was obtained under these conditions (Fig.2).

Transmission electron micrographs of the sample $WO_{2.9}$ + 0% Ta_2O_5 (Fig. 3) clearly reveal the intergrowth character of the crystal structure. The main spacing between crystallographic

shear planes (dark in Fig. 3) is ~2.36 nm in agreement with the crystal structure of $WO_{2.9}$ (Fig. 1). Non-uniform spacings of the shear planes indicate the incipient formation of $WO_{2.96}$.

The addition of Ta_2O_5 to the starting mixture may lead to the formation of solid solutions (e.g. $W_{1-x}Ta_xO_{2.90}$) and/or the formation of new ternary W-Ta-O Magnéli phases. Careful analysis of the powder XRD patterns did not reveal any additional reflections besides those belonging to binary Magnéli phases $WO_{2.90}$ and $WO_{2.96}$. Therefore, the tantalum seems to substitute tungsten in the Magnéli phase according to

$$1.6\ WO_3 + 0.2\ Ta_2O_5 = 2\ W_{0.8}Ta_{0.2}O_{2.90} \qquad (2)$$
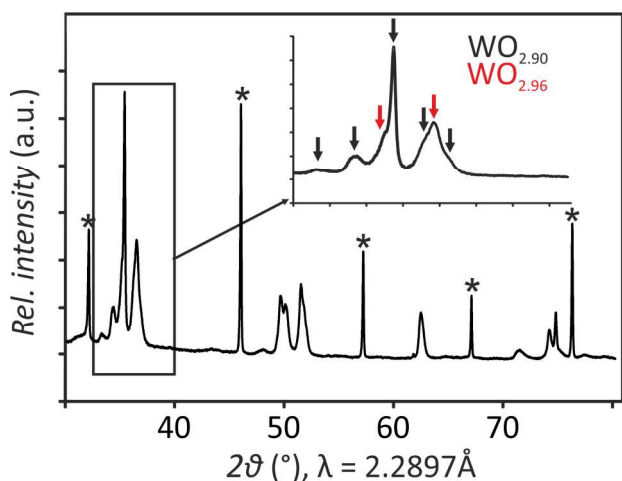
Fig. 2. Powder XRD pattern ($CrK_{\alpha1}$ radiation) of the products of the SPS-treated mixture $2.9WO_3 + 0.1W$. The reflections of the LaB_6 standard are marked by asterisks.
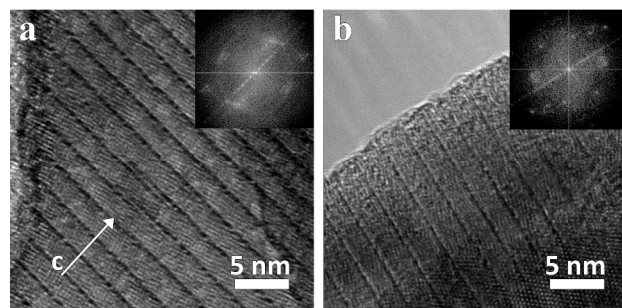
Fig. 3. Transmission electron micrographs of the reference sample $WO_{2.90}$ (0% Ta_2O_5) showing the intergrowth structure and the corresponding Fourier transform (FFT).

Because of the similar ionic radii of the W and Ta cations, the lattice parameters of $WO_{2.90}$ and the ternary samples are equal within 2-3 e.s.d. (binary: a = 12.060(3) Å, b = 3.7819(7) Å, c = 23.674(4) Å, β = 94.79(2)°; ternary (5 wt % of Ta_2O_5: a = 12.051(5) Å, b = 3.7796(7) Å, c = 23.648 (7) Å, β = 94.80(3)°).

Ta is not distributed homogeneously in the ternary phase. Detailed microstructure analysis of the pellets revealed increasing amounts of inclusions with increasing amounts of Ta_2O_5 (Fig. 4). The areas were identified as elemental tungsten, presumably originating from non-reacted starting material (zone III in Fig. 5 c, d) as a support for reaction (2) to occur. These inclusions are surrounded by a shell with varying W:O ratio (zone II in Fig. 5c, d). Zone II presents the intermediate products of the diffusion-controlled SPS-reaction between W and WO_3 similar as reported

previously for SPS-prepared Ti_2O_3. Both zones II+III are embedded in a $WO_{2.90}$ matrix (zone I), which presents the targeted product. In samples containing Ta_2O_5 in the starting mixture an additional minority phase was present (Fig. 5a, b). Elemental mapping of these regions (Fig. 5b) clearly revealed W-rich (red) and Ta-rich (green) grains. The Ta containing areas are distributed inhomogeneously in the material, and they are too small to allow a quantitative analysis. The absence of Ta in zones I-III also underlines inhomogeneous distribution of Ta and competing character of reactions (1) and (2).
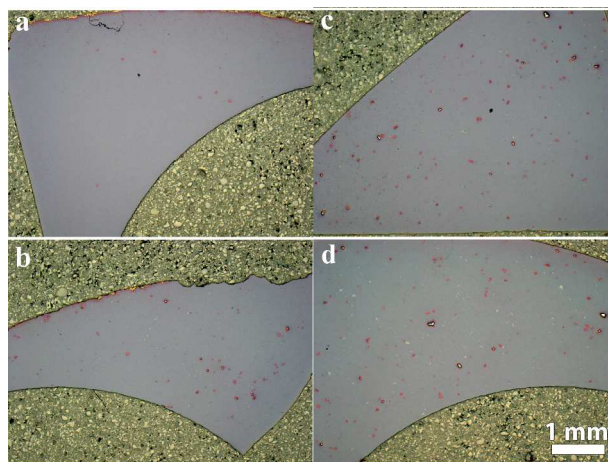
Fig. 4. Microstructure of the SPS sintered samples: (a) $WO_{2.90}$; (b) $WO_{2.90}$ + 3 mass % of Ta_2O_5; (c) $WO_{2.90}$ + 4 mass % of Ta_2O_5; (d) $WO_{2.90}$ + 5 mass % of Ta_2O_5. The black-formed inclusions contain tungsten and products of its reaction with WO_3, the reddish colored particles are formed by reaction of Ta_2O_5 with WO_3.
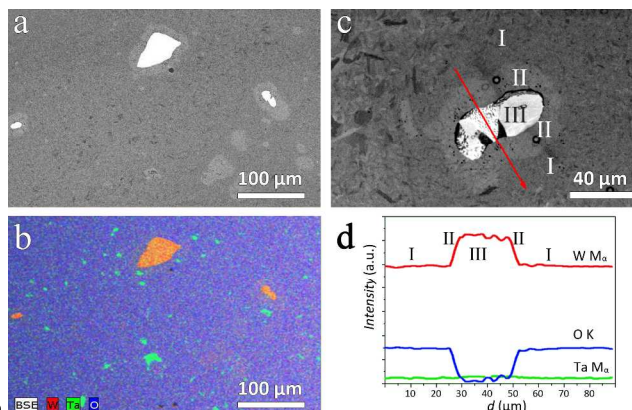
Fig. 5. Microstructure of the sample $WO_{2.90}$ + 5% Ta_2O_5: (a) background electron image revealing spatial distribution of the majority and minority phases; (b) element mapping of the region showed in (a); (c) magnified region around the tungsten-only nucleus; (d) line scans of the element content along the red line in (c).

Higher complexity of the microstructure of tantalum-containing specimens in comparison to tantalum-free samples is confirmed by TEM studies. In addition to the μm sized inclusions (Fig. 4, Fig. 5) the TEM images of the sample $WO_{2.90}$ + 5% Ta_2O_5 exhibit multiple inclusions with sizes between 5 nm and 50 nm (Fig. 6) In total, the microstructure of the SPS-manufactured samples $WO_{2.90} - x\%\ Ta_2O_5$ can be seen as a three-dimensionally organized system of (*i*) a not completely reacted starting component W and (*ii*) a ternary $W_{1-x}Ta_xO_{2.90}$ phase in a matrix of the target

phase $WO_{2.90}$. The non-reacted tungsten particles are spatially separated and surrounded by intermediates of the diffusion-controlled reaction (1). With the increasing amount of Ta_2O_5 in the starting mixture the number of tungsten inclusions increases due to reaction (2), i.e. the formation of a Ta-substituted Magnéli phase is preferred. The inclusions of both types of inclusions affect the thermal conductivity of the tantalum-containing samples (cf. below).
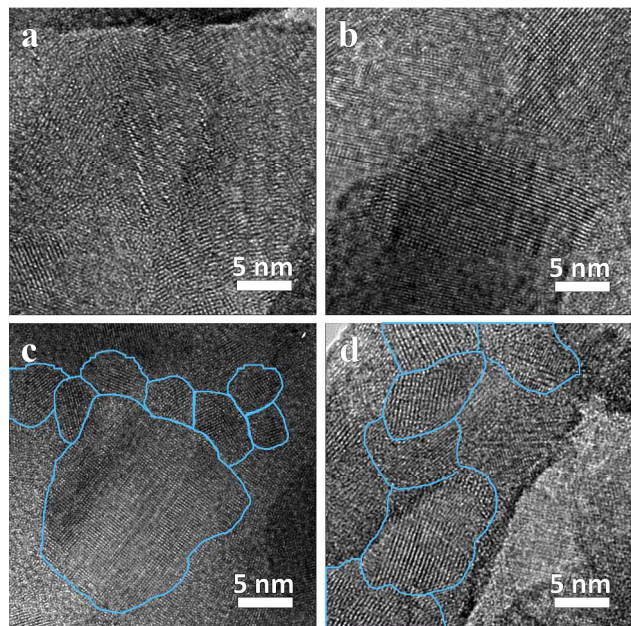
Fig. 6. TEM images of the sample $WO_{2.90}$ 5% of Ta_2O_5. Single crystal-line areas are highlighted in (c) and (d).
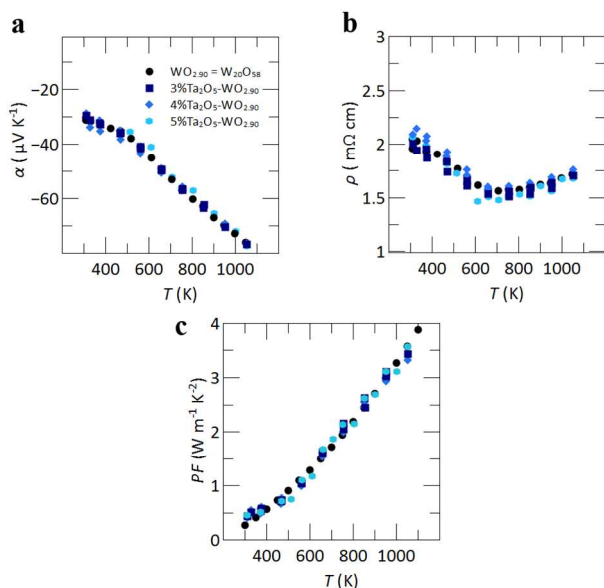
Fig. 7. (a) Temperature dependence of the thermopower α, (b) electrical resistivity ρ, and (c) power factor of $WO_{2.90}$ + x% Ta_2O_5 samples. Both, thermopower and electrical resistivity, are insensitive towards the Ta_2O_5 content, as typical for a heavily doped semiconductor.

The temperature dependences of the thermopower α and the electrical resistivity ρ (Fig. 7a,b), measured between room temperature and 1100 K, show the typical behavior of a heavily doped semiconductor. The resulting power-factors (Fig. 7c) are about one magnitude lower than current n-type oxide state of the art materials,[36] but the electronic transport properties are insensitive to the Ta_2O_5 content. The maximum of α is not yet reached at 1100 K, in harmony with a report on $WO_{2.90}$.[25]
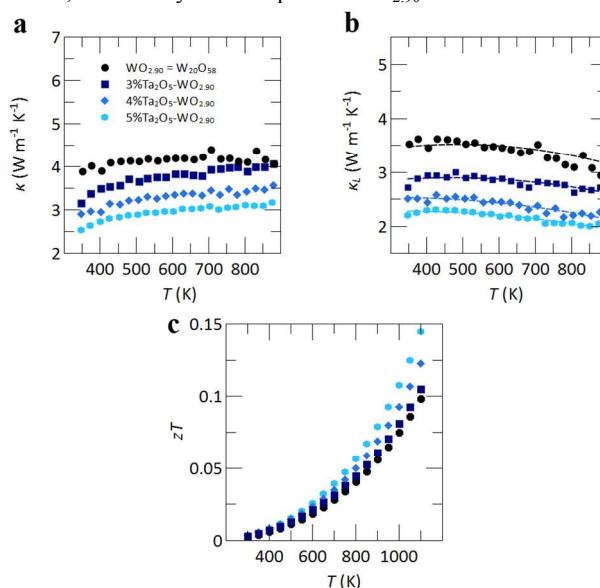
Fig. 8. Temperature dependence of the thermal conductivity κ **(a)**; the lattice thermal conductivity κ_{lat}, **(b)** calculated according to the Wiedemann-Franz law and of the calculated figure of merit zT **(c)**. The thermal conductivity above 900 K was extrapolated up to 1100 K.

The effect of the microstructure on thermal transport can qualitatively be understood within the Debye model of a phonon-gas.[42] In the absence of bipolar contributions, the absolute thermal conductivity contains in a first approximation an electronic and a lattice contribution.

$$\kappa = \kappa_{el} + \kappa_{lat} \tag{3}$$

As the electronic transport properties relevant for κ_{el} were unaffected by the addition of Ta_2O_5, the difference in κ can only be attributed to differences in κ_{lat} arising from the microstructure. The insensitivity of the electronic transport properties towards the Ta_2O_5 content is surprising as grain boundaries are effective scattering centres for charge carriers as well. This can be related to the fact that both types of inclusions in the $WO_{2.90}$ matrix are not interconnected in the microstructure.

The lattice part of the thermal conductivity was calculated from the Wiedemann-Franz law according to

$$\kappa_{el} = L\sigma T \tag{4}$$

assuming a Lorentz number of $L = 2.00 \cdot 10^{-8}$ W Ω K^{-2}. The resulting temperature dependence of κ_{lat} is presented in Figure 8b. Following the Debye's theory of a phonon-gas, κ_{lat} can be expressed as

$$\kappa_{lat} = \frac{1}{3}Cvl = \frac{1}{3}Cv^2\tau \tag{5},$$

neglecting the frequency dependence of the different parameters; C is the heat capacity of the compound, v the phonon velocity, l the mean free path and τ relaxation time of the phonons. The phonon relaxation time is related to l through the phonon veloci-

ty, $l = \tau \nu$ and can be written as the sum of all single scattering relaxation times, τ^{-1} of the different scattering processes i (Matthiessen's rule):

$$\tau^{-1} = \sum \tau_i^{-1} \qquad (6)$$

In the context of this work, contributions of Umklapp scattering τ_U^{-1}, grain boundary scattering τ_{GB}^{-1} and point defect scattering τ_{PD}^{-1} must be considered.[42,43] In general, Umklapp scattering becomes significant above the Debye temperature, but due to the high Debye temperature of $WO_{2.90}$ +x % Ta_2O_5 samples (T_D = 600 K), a clear T^{-1} behaviour of κ_{lat} cannot be determined in the temperature range examined here. However, for every sample shown in Fig. 8b, κ_{lat} decreases with increasing temperature. We attribute the decrease of κ_{lat} with increasing Ta_2O_5 content to enhanced phonon scattering at grain-boundaries of inclusion defects of a large size scale (Fig. 3-6), introducing scattering as a special feature for these materials.[2] Increased grain boundary scattering τ_{GB}^{-1} directly influences the mean free path of the phonons reducing thereby κ_{lat}. As point defect scattering is usually less dominant (or nearly non-existent at higher temperatures[34]) and because the differences of κ_{lat} are constant (Fig. 8b), additional contributions of point defect scattering can be neglected. Consequently, increasing amounts of Ta_2O_5 lead to a decrease of the thermal conductivity and, in turn, an increase of the figure of merit. Within this study $WO_{2.90}$ +5 % Ta_2O_5 shows the largest figure of merit zT = 0.15 at 1100 K (Fig 8c).

Conclusions

Spark plasma sintering (SPS) -assisted preparation and densification is a useful tool for large scale-preparation of the Magnéli phases. Achieving single-phase Magnéli oxides through conventional solid-state preparation implies long reaction times and powders require consolidation for measuring their physical properties. By starting the preparation from commercially available metal and metal oxide precursors, this work emphasizes the role of SPS for chemical tuning and optimized sintering to prepare superior thermoelectric materials. Crystallographic shear planes and defects on the sub-nanoscale were identified by HRTEM. In addition, the thermal conductivity of the Magnéli–type phase $WO_{2.90}$ was tuned via the underlying microstructure. By "alloying" Ta_2O_5 into the WO_3/W reaction mixture a concurrent reaction between WO_3 and Ta_2O_5 occurred during the SPS treatment, which lead to different types of inclusions: elemental tungsten from non-reacted starting material surrounded by a shell with variable W:O ratio, which represents the intermediate product of a diffusion-controlled SPS-reaction between the W and WO_3 precursors. These inclusions serve as micro-size scattering centers embedded in a $WO_{2.90}$ matrix. As a result, the thermal conductivity of the Ta-containing samples was reduced by approx. 30% over the measured temperature range through phonon scattering by shear planes and micro-size inclusions. As the electronic properties remained unaffected by the substitution the thermoelectric performance was enhanced with a maximum figure of merit of 0.15 at 1100 K. The electrical conductivity combined with a low lattice thermal conductivity - caused by the crystal structure at the nano- and inclusions at the microscale - makes Magnéli phases an interesting class of materials for thermoelectric research. This report - together with ref. 3 - describes a first approach to systematically control their thermal (and electronic) transport properties. This knowledge is not only relevant for tungsten-based Magnéli-type oxides but also for an optimization of other metal oxides for thermoelectric applications.

Notes and references

aInstitut für Anorganische Chemie und Analytische Chemie der Johannes Gutenberg-Universität, Duesbergweg 10-14, D-55099 Mainz, Germany
bMax-Planck-Institut für Chemische Physik fester Stoffe, Nöthnitzer Str. 40, 01187 Dresden, Germany
cMaterials Research Laboratory, University of California, Santa Barbara, California, 93106, USA
dDepartment of Chemistry and Biochemistry, University of California, Santa Barbara, California, 93106, USA
eMaterials Department, University of California, Santa Barbara, California, 93106, USA
fMax-Planck-Institut für Polymerforschung, Ackermannweg, 55128 Mainz, Germany
*Corresponding Authors: E-Mail: tremel@uni-mainz.de (WT), grin@cpfs.mpg.de (YG)

1   M. Zebarjadi, K. Esfarjani, M. S. Dresselhaus, Z. F. Ren, and G. Chen, *Energy Environ. Sci.* 2012, **5**, 5147-5162.
2   K. Biswas, J. He, I. D. Blum, C.-I. Wu, T. P. Hogan, D. N. Seidman, V. P. Dravid, and M. G. Kanatzidis, *Nature* 2012, **489**, 414–418.
3   C. Liu, L. Miao, J. Zhou, R. Huang, C. A. J. Fisher, and S. Tanemura, *J. Phys. Chem. C* 2013, **117**, 11487–11497.
4   Y. Lan, A. J. Minnich, G. Chen, and Z. Ren, *Adv. Funct. Mater.* 2010, **20**, 357–376.
5   T. C. Harman, P. J. Taylor, M. Walsch, and B. LaForge, *Science*, 2002, **297**, 2229–2232.
6   W. G. Zeier, A. LaLonde, Z. M. Gibbs, C. P. Heinrich, M. Panthöfer, G. J. Snyder, and W. Tremel, *J. Am. Chem. Soc.* 2012, **134**, 7147–7154.
7   W. Liu, X. Yan, G. Chen and Z. Ren, *Nano Energy* 2012, **1**, 42–56.
8   M. S. Dresselhaus, G. Chen, M. Y. Tang, R. G. Yang, H. Lee, D. Z. Wang, Z. F. Ren, J.-P. Fleurial, and P. Gogna, *Adv. Mater.* 2007, **19,** 1043–1053.
9   Y. Pei, J. Lensch-Falk, E. S. Toberer, D. L. Medlin, and G. J. Snyder, *Adv. Funct. Mater.* 2011, **21**, 241–249.
10 J. P. Heremans, V. Jovovic, E. S. Toberer, A. Saramat, K. Kurosaki, A. Charoenphakdee, S. Yamanaka, and G. J. Snyder, *Science,* 2008, **321**, 554–557.
11 K. F. Hsu, S. Loo, W. Chen, J. Dyck, C. Uher, T. Hogan, E. K. Polychroniadis, and M. G. Kanatzidis, *Science* 2004, **303**, 818–821.
12 E. A. Skrabek and D. Trimmer, In *CRS Handbook of Thermoelectrics*, ed. Rowe, D. M., pp. 267–275.
13 B. Poudel, Q. Hao, Y. Ma, Y. Lan, A. Minnich, B. Yu, X. Yan, D. Wang, A. Muto, D. Vashaee, X. Chen, J. Liu, M. S. Dresselhaus, G. Chen, and Z. Ren, *Science* 2008, **320**, 634–638.

14   W. Liu, K. C. Lukas, K. McEnaney, S. Lee, Q. Zhang, C. P. Opeil, G. Chen and Z. Ren, *Energy Environ. Sci.* 2013, **6**, 552-560.

15   G. J. Snyder and E. S. Toberer, *Nat Mater.* 2008, **7**, 105–114.

16   H. Zhang, H. Borrmann, N. Oeschler, C. Candolfi, W. Schnelle, M. Schmidt, U. Burkhardt, M. Baitinger, J.-T. Zhao, and Yu. Grin. *Inorg. Chem.* 2011, **50**, 1250-1257.

17   S. Harada, K. Tanaka, and H. Inui, *J. Appl. Phys.* 2010, **108**, 83703.

18   D. Portehault, V. Maneeratana, C. Candolfi, N. Oeschler, I. Veremchuk, Yu. Grin, C. Sanchez, and M. Antonietti, *ACS Nano,* 2011, **5**, 9052–9061.

19   C. Chiritescu, D. G. Cahill, N. Nguyen, D. C. Johnson, A. Bodapati, P. Keblinski, and P. Zschack, *Science* 2007, **315**, 351-353.

20   Q. Lin, M. Smeller, C. L. Heideman, P. Zschack, M. Koyano, M. D. Anderson, R. Kykyneshi, D. A. Keszler, I. M. Anderson, and D. C. Johnson, *Chem. Mater.* 2010, **22**, 1002-1009.

21   A. Magnéli, B. Blomberg-Hansson, L. Kihlborg, and G. Sundkvist, *Acta Chem. Scand.* 1955, **9**, 1382–1390.

22   K. Fuda, T. Shoji, S. Kikuchi, Y. Kunihiro, and S. Sugiyama, *J. Elec. Mater.* 2013, **42**, 2209–2213.

23   M. Backhaus-Ricoult, J. R. Rustad, D. Vargheese, I. Dutta, and K. Work, *J. Electr. Mater.* 2012, **41**, 1636–1647.

24   J. M. Berak and M. Sienko, *J. Sol. State Chem.* 1970, **2**, 109–133.

25   G. Kieslich, I. Veremchuck, I. Antonyshyn, W. G. Zeier, C. Birkel, Yu. Grin and W. Tremel, *Phys. Chem. Chem. Phys.* 2013, **15,** 15399-15403.

26   D. R. Clarke, *Surf. Coat. Technol.* 2003, **163-164**, 67–74.

27   J. Dolinšek, M. Komelj, P. Jeglič, S. Vrtnik, D. Stanić, P. Popčević, J. Ivkov, A. Smontara, Z. Jagličić, P. Gille, and Yu. Grin, *Phys. Rev. B* 2009, **79**. 184201.

28   P. Popčević, A. Smontara, J. Ivkov, M. Wencka, M. Komelj, P. Jeglič, S. Vrtnik, M. Bobnar, Z. Jagličić, B. Bauer, P. Gille, H. Borrmann, U. Burkhardt, Yu. Grin, and J. Dolinšek, *Phys. Rev. B* 2010, **81**, 184203.

29   J. Dolinšek and A. Smontara, *Isr. J. Chem.* 2011, **51**, 1246–1256.

30   E. S. Toberer, A. Zevalkink, and G. J. Snyder, *J. Mater. Chem.* 2011, **21**, 15843.

31   M. W. Gaultois, T. D. Sparks, C. K. H. Borg, R. Seshadri, W. D. Bonificio, and D. R. Clarke, *Chem. Mater.* 2013, **25**, 2911–2920.

32   G. Slack Solid State Physics, Academic Press, New York, 1979.

33   G. Kieslich, C. S. Birkel, J. E. Douglas, M. Gaultois, I. Veremchuk, R. Seshadri, G. D. Stucky, Yu. Grin, and W. Tremel, *J. Mater. Chem. A* 2013. **1**, 13050-13054.

34   R. Tilley, *Int. J. Refract. Met. Hard Mater.* 1995, **13**, 93–109.

35   A. Polaczek, M. Pekala, and Z. Obuszko, *J. Phys.: Condens. Matter.* 1994, **6**, 7909–7919.

36   M. Ohtaki, K. Araki, K. Yamamoto, *J. Electron. Mater.* 2009, **7**, 1234-1238.

37   K. Koumoto, Y. Wang, R. Zhang, A. Kosuga, R Funahashi, *Annu. Rev. Mater.* Res. 2010, **40**, 363-394.

38   N. M. G. Parreira, T. Polcar, A. Cavaleiro, *Surface and Coatings Technol.* 2007, **201**, 7076-7082.

39   I. Veremchuk, I. Antonyshyn, C. Candolfi, X. Feng, U. Burkhardt, M. Baitinger, J.-T. Zhao, and Yu. Grin. *Inorg. Chem.* 2013, **52**, 4458–4463.

40   E. Gebert and R. J. Ackermann, *Inorg. Chem.* 1966, **5**, 136-142.

41   L. Akselrud and Yu. Grin, *J. Appl. Crystallogr.* 2014, **47**, 803-805.

42   J. M Ziman, Electrons and Phonons, Oxford University Press, New York, 1960

43   J. Booth, T. Ekström, E. Iguchi, and R. Tilley, *J. Solid State Chem.* 1982, **41**, 293–307.

Journal of Materials Chemistry A Accepted Manuscript